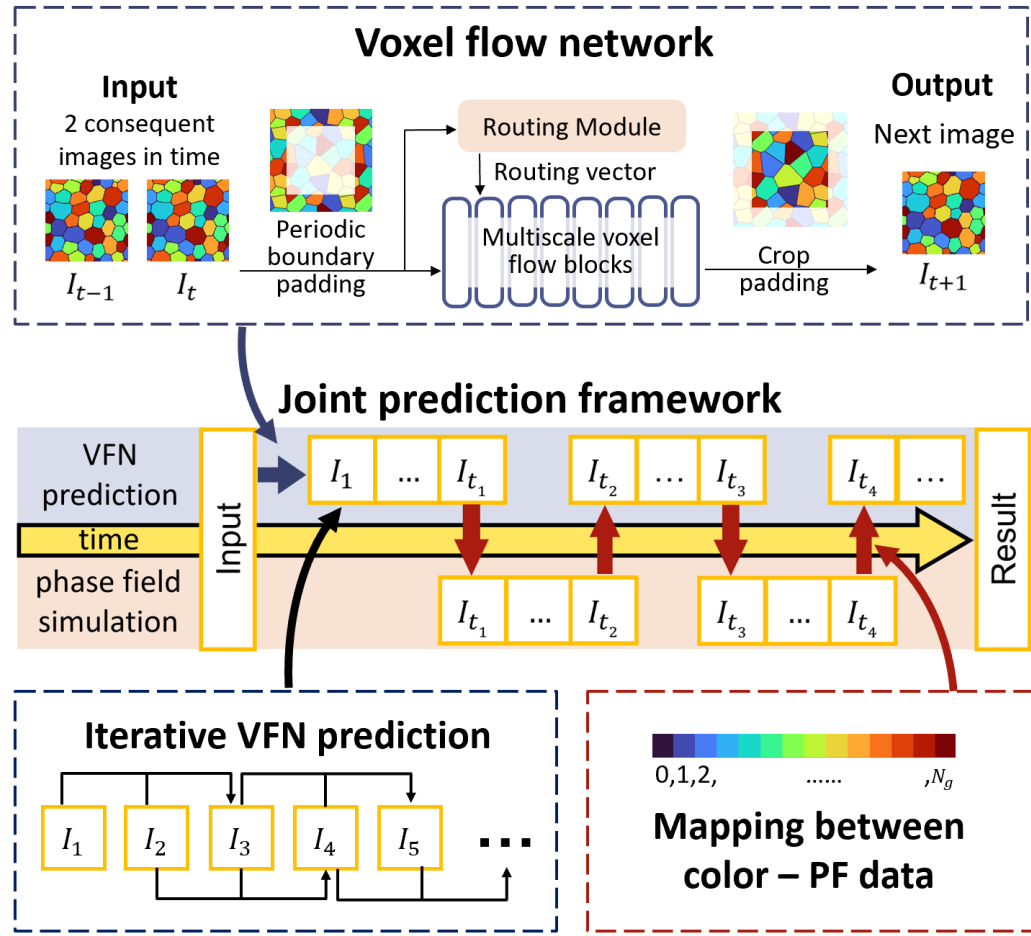


Graphical Abstract

A Joint Voxel Flow-Phase Field Framework for Ultra-Long Microstructure Evolution Prediction with Physical Regularization

Ao Zhou, Salma Zahran, Chi Chen, Zhengyang Zhang, Yanming Wang



Highlights

A Joint Voxel Flow-Phase Field Framework for Ultra-Long Microstructure Evolution Prediction with Physical Regularization

Ao Zhou, Salma Zahran, Chi Chen, Zhengyang Zhang, Yanming Wang

- A joint framework unites voxel flow network and phase-field for evolution prediction.
- Physical regularization in the framework controls error of prediction results.
- The framework enables stable and ultra long microstructure evolution prediction.
- The method was validated on grain growth and spinodal decomposition benchmarks.
- High accuracy, strong generalization, and notable computational speedup are achieved.

A Joint Voxel Flow-Phase Field Framework for Ultra-Long Microstructure Evolution Prediction with Physical Regularization

Ao Zhou^a, Salma Zahran^a, Chi Chen^a, Zhengyang Zhang^{a,b,***}, Yanming Wang^{c,*}

^a*Global College, Shanghai Jiao Tong University, Shanghai, 200240, China*

^b*Xiaomi Company, Beijing, China*

^c*Global Institute of Future Technology, Shanghai Jiao Tong University, Shanghai, 200240, China*

Abstract

Phase-field (PF) modeling is a powerful tool for simulating microstructure evolution. To overcome the high computational cost of PF in solving complex PDEs, machine learning methods such as PINNs, convLSTM have been used to predict PF evolution. However, current methods still face shortages of low flexibility, poor generalization and short predicting time length. In this work, we present a joint framework coupling voxel-flow network (VFN) with PF simulations in an alternating manner for long-horizon temporal prediction of microstructure evolution. The VFN iteratively predicts future evolution by learning the flow of pixels from past snapshots, with periodic boundaries preserved in the process. Periodical PF simulations suppresses nonphysical artifacts, reduces accumulated error, and extends reliable prediction time length. The VFN is about 1,000 times faster than PF simulation on GPU. In validation using grain growth and spinodal decomposition, MSE and SSIM remain 6.76% and 0.911 when predicted 18 frames from only 2 input frames, outperforming similar predicting methods. For an ultra-long grain growth prediction for 82 frames from 2 input frames, grain number decreases from 600 to 29 with NMSE of average grain area remaining 1.64%. This joint framework enables rapid, generalized, flexible and physically consistent microstructure forecasting from image-based data for ultra-long time

*yanming.wang@sjtu.edu.cn

**zhangzhengyang3@xiaomi.com

scales.

Keywords: Phase field model, Voxel flow network, Machine learning, Acceleration method, Microstructure evolution prediction

1. Introduction

Phase-field models [1] are widely used to simulate microstructure evolution in various materials, including sintering [2], grain growth [3], dendrite solidification and deposition [4, 5], and spinodal decomposition [6]. These models, governed by partial differential equations (PDEs), offer a robust framework for capturing the complex dynamics of phase transitions. Despite their predictive power, phase-field models can be computationally expensive and time-consuming [7], particularly when simulating the evolution over long periods or across large domains. To address these challenges, recent studies have integrated machine learning (ML) techniques with phase-field simulations to accelerate computation [8, 9]. Broadly, two types of approaches have emerged: physics-informed methods, such as physics-informed neural networks (PINNs) [10], which aim to solve the governing PDEs more efficiently; and purely data-driven methods, which bypass PDE solving entirely by learning the evolution directly from data [11]. The former focuses on embedding physical laws into neural architectures to preserve fidelity, while the latter emphasizes flexibility and speed, relying on high-quality simulation or experimental data to capture spatiotemporal patterns.

Physics-informed neural networks (PINNs) incorporate physical laws, typically expressed as partial differential equations, directly into the learning process by embedding the governing equations into the loss function [10]. Unlike purely data-driven approaches, PINNs optimize both the mismatch between predicted data and ground truth and the residuals of physical equations such as the Allen–Cahn and Cahn–Hilliard equations [12, 13], with spatial and temporal derivatives computed via automatic differentiation to enforce physical consistency. Motivated by their potential to accelerate phase-field simulations, numerous extensions have been proposed to improve accuracy and convergence, including hard enforcement of initial and boundary conditions [14], advanced sampling strategies with NTK-based adaptive loss weighting in PF-PINNs [15], and time-marching PINN formulations for coupled Cahn–Hilliard–Navier–Stokes systems [16]. Further efforts have addressed multi-phase problems through PINNs-MPF [17] and PINN-Phase,

which leverages transfer learning and ConvLSTM acceleration [18], while more recent physics-informed neural operators, such as DeepONet [19] and Fourier-domain PINOs [20], aim to reduce computational overhead by reformulating the learning paradigm. Despite these advances, physics-informed methods generally require careful loss balancing, extensive training, and explicit knowledge of the governing equations, leading to limited scalability and efficiency for long-time integration and large-scale microstructure evolution; moreover, their flexibility is fundamentally constrained by the need for pre-defined phase-field models. While PINNs have demonstrated high precision for problems such as spinodal decomposition [21], they are less suitable for applications driven purely by experimental data or raw images, where no explicit physical model is available. In addition, PINNs typically demand problem-specific network architectures and customized loss formulations for each phase-field system, severely limiting their generalizability; this issue becomes especially pronounced for complex multi-phase-field models, where the number of coupled evolution equations increases substantially. For example, the grain growth phase-field model employs multiple order parameters, each governed by a separate Allen–Cahn equation [3], which would require a highly complex composite loss function to enforce all coupled dynamics simultaneously—a formulation that has not yet been demonstrated in the literature. Consequently, grain growth prediction has largely been pursued using graph neural network-based methods rather than PINNs.

Another class of machine learning approaches directly learns microstructure evolution from data, including convolutional neural networks (CNNs), recurrent neural networks (RNNs), long short-term memory networks (LSTMs), and graph neural networks (GNNs). Convolutional recurrent neural networks (CRNNs) have been successfully applied to predict spinodal decomposition, including three-dimensional evolution with physics-inspired architectures that enable long-term extrapolation [11, 22]. CNN-based frameworks, often combined with recurrent structures, have also been used to model phase-field evolution in dendritic growth, grain growth, and spinodal decomposition [23, 24]. More recently, graph neural networks have demonstrated improved predictive capability for grain growth by explicitly modeling topological relationships, outperforming CNN-based methods [25]. In addition, a dynamic GNN model, called GrainGNN, was developed for 3D epitaxial grain growth [26]. Further advancements have integrated LSTMs with CNNs or RNNs for prediction tasks, including using in-situ SEM images to predict microstructure evolution [27, 28, 29]. Some works have explored

low-dimensional representations, employing RNNs, LSTMs [30, 31], or deep neural operators to model spinodal decomposition [32]. Other architectures, such as ResNet, U-Net, and Y-Net, have also been used to predict phase-field evolution for various processes, including dendrite growth [33, 34], spinodal decomposition [35, 36, 37], and grain growth [38]. Despite these advances, most models are purely data-driven prediction models, and they struggle with accuracy for long time range predictions beyond the time length of their training dataset. This limits their broader application in real-world scenarios. In addition, existing grain growth prediction studies typically use binary-colored images, which makes it difficult to distinguish and track individual grains and limits the effectiveness of post-processing analyses.

Since the microstructure evolution is also a sequence of images in time direction, it is natural to modify the most recent and powerful video prediction models to predict phase field evolution. One example showed the result of using SimVP video prediction model [39] combined with multi-order aggregation features to build a model called "SimGate" [40] predict sintering of polycrystalline particles. Another type of video prediction method called optical flow method predicts future video frames by finding the movement of pixels in neighboring frames, achieving light weighted while powerful prediction capability. Voxel flow network [41] is a kind of optical flow method that predicts the next frame of video from two previous frames. It gives end-to-end prediction by predicting the per-pixel motion between adjacent frames, and dynamically adjust a scaling factor to capture motion in different scales while maintaining the correct spatial information. Considering the time evolution of phase field models also has different scales of motion, it could be beneficial to integrate VFN and phase field predictions.

Considering the challenges of current prediction methods and the potential benefit of VFN, we choose to create a joint prediction framework that combines VFN and physical error correction for longer horizon, generalized phase field predictions. The VFN is used for rapid prediction of microstructure evolution, while short phase-field simulations are periodically inserted to correct accumulated prediction errors. Unlike traditional methods that solve PDEs or extract intermediate features, our approach treats evolving microstructures as a sequence of video frames, directly learning the spatiotemporal evolution from the pixel-level dynamics of phase-field images. We adopt colored phase-field configuration snapshots, in contrast to previous studies that rely on binary coloring, which facilitates seamless transfer between VFN prediction and phase-field simulation. By leveraging high-

fidelity phase-field simulations as training data, the VFN captures both local and global features of microstructure evolution with high accuracy. In the following sections, we will demonstrate the VFN prediction of grain growth and spinodal decomposition process, then use joint framework to predict long time scale grain growth evolution to show its robust ability to do prediction on various and long time range microstructure evolution.

2. Methods

2.1. Joint prediction framework

By treating microstructure evolution as a sequence of images, we formulate phase-field dynamics as a video prediction problem and develop a joint framework that couples data-driven voxel flow prediction with physics-based phase-field (PF) simulations. As illustrated in figure 1(b), the voxel flow network (VFN) and PF solver are alternately employed to predict long-term microstructure evolution. The VFN predicts successive microstructural frames directly from image inputs, while short PF simulation segments are periodically inserted to correct accumulated errors and maintain physical consistency. The linkage between images and phase-field variables is enabled by an image–data mapping procedure (figure 1(d)), which is described in detail below.

The joint prediction proceeds as follows. Starting from two consecutive images, the VFN iteratively predicts several future frames $I_1 \rightarrow I_{t_1}$. The phase-field configuration is then reconstructed from the final predicted image via the image–data mapping and used as the initial condition for a short PF simulation, producing frames $I_{t_1} \rightarrow I_{t_2}$. The last two PF snapshots are subsequently fed back into the VFN, which resumes prediction for the next segment $I_{t_2} \rightarrow I_{t_3}$. This alternating procedure can be repeated multiple times to reach arbitrarily long prediction horizons I_{t_4}, I_{t_5}, \dots . Because the time span available in the training data is finite, VFN-only prediction tends to accumulate errors when extrapolated far beyond the training range. By periodically inserting short corrective PF simulations, the joint framework effectively suppresses error growth and substantially extends the feasible prediction horizon.

The VFN architecture, shown in figure 1(a), consists of nine sequential voxel flow blocks (VFBs; Section 2.2) operating at progressively finer effective resolutions, together with a routing module (Section 2.3) that computes a routing vector for each prediction. Prior to VFN inference, input PF snapshot

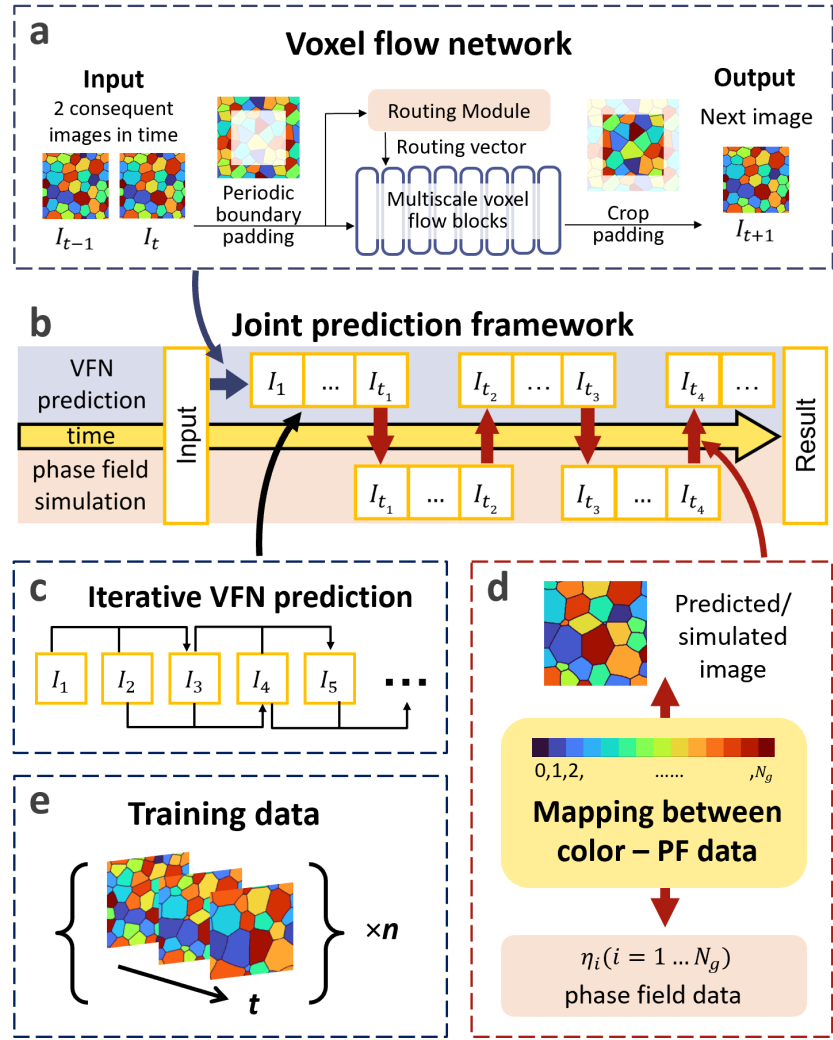


Figure 1: Method diagram of this work. (a) Voxel flow network with padding–cropping operation for enforcing periodic boundaries. (b) Joint prediction framework integrating voxel flow network and corrective phase-field simulations. (c) Iterative prediction procedure, where each predicted output frame is fed back as the next input. (d) Image–data interface based on colormap mapping between RGB pixels and phase-field variables. (e) Phase-field evolution image datasets for training and validation.

images are padded to enforce periodic boundary conditions. After prediction, the padded boundaries are discarded and only the central region is retained. The routing vector dynamically determines which VFB scales are activated based on the estimated motion magnitude between the two input frames [41]. Each VFB predicts incremental refinements to both the voxel flow and the blending mask, while the routing mechanism adaptively selects the relevant refinement stages during training and inference. This design enables efficient allocation of computational resources by executing only the necessary blocks for a given input while maintaining high predictive accuracy.

Given two consecutive input frames I_{t-1} and I_t , the VFN predicts the next frame I_{t+1} , which is then recursively fed back as input to generate longer trajectories (figure 1(c)). Specifically, the network estimates backward optical flows $f_{t+1 \rightarrow t}$ and $f_{t+1 \rightarrow t-1}$, which map pixels from the predicted frame to the two preceding frames. Using pixel-wise backward warping, denoted by $\overleftarrow{W}(\cdot)$, and a fusion mask m that accounts for discontinuous motion such as occlusion or newly exposed regions, the predicted frame is reconstructed as

$$I_{t+1} = m \times \overleftarrow{W}(I_{t-1}, f_{t+1 \rightarrow t-1}) + (1 - m) \times \overleftarrow{W}(I_t, f_{t+1 \rightarrow t}). \quad (1)$$

For notational convenience, we denote the collection of optical flows and the fusion mask as the voxel flow F_{t+1} . Equation (1) can then be compactly written as

$$I_{t+1} = \overleftarrow{W}(I_{t-1}, I_t, F_{t+1}), \quad (2)$$

indicating that predicting I_{t+1} reduces to estimating the voxel flow F_{t+1} .

To enable joint simulation and quantitative analysis, we introduce a forward–reverse colormap mapping between images and underlying phase-field configurations, as illustrated in figure 1(d). For the grain growth model, each color in the turbo colormap corresponds to a distinct grain order parameter $\eta_i \in [0, 1]$, $i = 1, 2, \dots, N_g$, where N_g is the total number of grains. In the forward mapping, a grain index matrix with values $\{0, 1, 2, \dots, N_g\}$ is constructed, where 0 denotes grain boundaries, and each index is mapped to an RGB value using the colormap. To reconstruct phase-field data from predicted images, a reverse mapping is performed: for each pixel, its RGB value is compared with the colormap using the Euclidean distance in RGB space, and the closest match i is selected to recover $\eta_i = 1$ and $\eta_j = 0$ for $j \neq i$. For spinodal decomposition, reconstruction is simpler, as the concentration field is obtained by interpolating the RGB values along the colormap to the interval $(0, 1)$. This forward–reverse mapping establishes a bijective

correspondence between phase-field data and image representation, enabling seamless transitions between simulation and prediction and ensuring that predicted images can be analyzed in the same manner as PF simulation outputs.

2.2. Voxel flow blocks

The VFB is designed to refine voxel flow estimates in an end-to-end manner while avoiding restrictive assumptions such as locally linear or temporally symmetric motion. Given two consecutive input phase field snapshot frames I_{t-1} and I_t , a synthesized intermediate prediction frame \tilde{I}_{t+1}^{i-1} , and the voxel flow predicted by the previous block F_{t+1}^{i-1} , the i -th VFB learns to approximate the target voxel flow F_{t+1}^i . The initial block starts from $\tilde{I}_{t+1}^0 = 0$ and $F_{t+1}^0 = 0$, and a sequence of nine VFBs is used to produce the final future frame. The detail of VFB is described in algorithm 1.

To effectively capture both large-scale motion and fine spatial structures, each VFB uses a two-branch architecture inspired by pyramidal optical-flow estimation. The motion branch operates on a downsampled version of the input PF snapshot frames, expanding the receptive field for large displacements. For the i -th block, a scaling factor $S_i \in \{4, 4, 4, 2, 2, 2, 1, 1, 1\}$ is used, and both the input PF frames and the incoming voxel flow are rescaled by $1/S_i$. After feature extraction via two strided convolutions and residual convolutional blocks, the resulting motion features are compressed using a squeeze convolution and subsequently upsampled by a factor of $2S_i$.

In parallel, a spatial branch processes the original-resolution inputs using a light convolutional stack, preserving local textures and structural cues. The features from the two branches are concatenated and decoded using a transposed convolution to produce a 5-channel output comprising a refined voxel flow and a soft blending mask. This design allows each block to progressively refine motion estimates while maintaining spatial fidelity.

Across all nine VFBs, the receptive field grows naturally due to multiscale downsampling, while the spatial branch ensures that high-frequency details are retained. This coarse-to-fine refinement strategy enables the model to handle large, nonlinear, or asymmetric motions without the need for explicit flow linearization, symmetry assumptions, or flow-reversal layers.

2.3. Routing mechanism and VFN architecture

The VFN predicts future PF evolution frames by progressively refining a voxel flow field through a sequence of nine VFBs. The output of each VFB

Algorithm 1: Multiscale Voxel Flow Block (VFB)

Input: Input frames I_{t-1}, I_t , previous synthesized frame \tilde{I}_{t+1}^{i-1} ,

previous voxel flow F_{t+1}^{i-1} , scale factor S_i

Output: Refined voxel flow F_{t+1}^i , blending mask M^i

1. Input preparation:

Concatenate inputs: $X \leftarrow [I_{t-1}, I_t, \tilde{I}_{t+1}^{i-1}]$, $F \leftarrow F_{t+1}^{i-1}$;

if $S_i \neq 1$ **then**

$X_d \leftarrow \text{Interp}(X, 1/S_i)$;
 $F_d \leftarrow \text{Interp}(F, 1/S_i)/S_i$;

else

$X_d \leftarrow X$, $F_d \leftarrow F$;

2. Motion branch (low resolution):

$H_1 \leftarrow \text{Conv}_{\downarrow}([X_d, F_d])$; // two strided conv layers

$H_2 \leftarrow \text{ConvBlock}(H_1) + H_1$; // three residual conv blocks

$H_s \leftarrow \text{Conv}_{sq}(H_2)$; // channel squeeze

$H_m \leftarrow \text{Interp}(H_s, 2S_i)$; // upsample to final scale

3. Spatial branch (full resolution):

$H_{sp} \leftarrow \text{Conv}([X, F])$;

$H_{sp} \leftarrow \text{ConvBlock}(H_{sp})$;

4. Fusion and decoding:

$H \leftarrow [H_m, H_{sp}]$; // feature fusion

$T \leftarrow \text{ConvTranspose}(H)$; // decode voxel flow + mask

5. Output splitting:

$F_{t+1}^i \leftarrow T[:, 1:4]$; // 4-channel voxel flow

$M^i \leftarrow T[:, 5]$; // 1-channel blending mask

return F_{t+1}^i, M^i

updates the current voxel flow estimate, which is then used to warp the input frames and synthesize an intermediate prediction.

To decide which scales of VFBs to go through during one inference, VFN incorporates a dynamic routing mechanism that adaptively selects a sub-network for each input pair. Motion complexity varies across different frame pairs, and full-depth computation is unnecessary for small-motion samples. VFN therefore introduces a lightweight Routing Module to predict a binary routing vector indicating which VFBs should be executed. This design allows up to 2^9 possible inference paths, enabling flexible computation tailored to input motion magnitude.

The Routing Module consists of two convolutional layers followed by global average pooling and a fully connected layer, producing a nine-dimensional probability vector \tilde{v} . A straight-through estimator samples a binary routing vector $v \in \{0, 1\}^9$, which determines which VFBs contribute updates to the voxel flow. During training, both activated and deactivated branches are averaged to maintain differentiability, while at inference only the activated blocks are executed. This dynamic strategy preserves representational capacity for large motions while significantly reducing computational cost for simpler inputs. The final synthesized frame is formed by warping the input frames with the refined voxel flow and blending them using the learned mask.

2.4. Dataset preparation and model training

To test the generalizability of our framework, we selected two phase-field model to build our database for training and validation of the framework: the grain growth model of L. Q. Chen [3] and the spinodal decomposition model of A. Cahn [6]. Evolution snapshots from these two models were used as training and validation datasets for our prediction framework. For one simulation, snapshots with same intervals in between are taken according to evolution time sequence, as the direction t shown in figure 1(e). For the grain growth model, the initial microstructure was generated using Voronoi tessellations, and a regularization method [42] with regularity parameter $\alpha = 0.8$ was used to make the grains generated with Voronoi tessellation have areas in a certain distribution for more realistic structures. Then the phase-field simulations were performed to obtain the subsequent evolution, with intervals of 1,000 steps. The model parameters of the grain growth snapshots were $L = 1$, $\Delta t = 0.2$, $\Delta x = 2$, $\kappa = 2$, $\alpha = 1$, $\beta = 1$, $\gamma = 1$. [3] The snapshots were visualized using the turbo colormap, in which colors were

Algorithm 2: Dynamic Routing and Forward Pass of VFN

Input: Input frames I_{t-1}, I_t , scaling factors $\{S_i\}_{i=1}^9$

Output: Synthesized future frame \tilde{I}_{t+1}

1. Routing prediction:

```
 $F \leftarrow 0, M \leftarrow 0, \tilde{I} \leftarrow 0;$  // initial voxel flow, mask, and frame
 $R \leftarrow \text{RoutingModule}(I_{t-1}, I_t);$  // two convs + avg pooling
 $\tilde{v} \leftarrow \sigma(\text{Linear}(R));$  // routing probabilities
 $v \leftarrow \text{RoundSTE}(\tilde{v});$  // binary routing vector
```

2. Iterative refinement through nine MVFB blocks:

for $i = 1$ to 9 do

 if *training* then

```
 $\Delta F_i, \Delta M_i \leftarrow \text{MVFB}_i([I_{t-1}, I_t, \tilde{I}, M], F; S_i);$ 
 $F_{\text{temp}} \leftarrow F + \Delta F_i, M_{\text{temp}} \leftarrow M + \Delta M_i;$ 
 $F \leftarrow F + v_i \cdot \Delta F_i;$  // weighted update
 $M \leftarrow M + v_i \cdot \Delta M_i;$ 
Compute warped frames using both  $F_{\text{temp}}$  and  $F$ ;
```

 else

```
        if  $v_i = 1$  then
             $\Delta F_i, \Delta M_i \leftarrow \text{MVFB}_i([I_{t-1}, I_t, \tilde{I}, M], F; S_i);$ 
             $F \leftarrow F + \Delta F_i, M \leftarrow M + \Delta M_i;$ 
```

 Warp I_{t-1} and I_t using the updated F to obtain \tilde{I} ;

3. Final synthesis:

$\tilde{I}_{t+1} \leftarrow \tilde{I} \cdot \sigma(M) + (1 - \sigma(M)) \cdot \text{opposing warp};$

return \tilde{I}_{t+1}

assigned according to the phase-field order-parameter index of each grain, following the color–phase-field data mapping strategy described in section 2.1. For the spinodal decomposition model, random initial configurations were employed, and images were likewise recorded at 1,000-step intervals. We used regular solution model as the Helmholtz free energy term, added with gradient energy, the free energy density writes:

$$f(c) = \ln c + \ln(1 - c) + \Omega c(1 - c) + \kappa(\nabla c)^2 \quad (3)$$

where $\Omega = 3.4$, $\kappa = 1$, for evolution, diffusivity $D = 0.05$ and $\Delta t = 0.1$. Periodic boundary conditions were applied in both simulations. Distinct random initial conditions were used to generate separate datasets for training and validation, as shown as $\times n$ in figure 1(e).

The framework was implemented and trained using the PyTorch framework [43] and all numerical operations and data handling were performed using NumPy [44]. The model was trained separately for grain growth and spinodal decomposition phase field models. For grain growth, we employed 300 PF simulations, each containing 20 images, with an additional 20 simulations reserved for validation. We trained the model for 1,500 epochs on a NVIDIA RTX A4000 GPU. The training batch size was 28 and a cosine annealing was used to reduce the learning rate from 10^{-4} to 10^{-5} . Training loss was designed as addition of l_1 loss and VGG loss. The l_1 loss was calculated on the Laplacian pyramid representations, and the total loss function was the sum of them, with parameter $\gamma = 0.8$:

$$L_{total} = \sum_{i=1}^n \gamma^{n-i} l_1(\tilde{I}_{t+1}^i, I_{t+1}) + 0.5 l_{VGG}(\tilde{I}_{t+1}^9, I_{t+1}) \quad (4)$$

The training loss plot of VFN on grain growth and spinodal decomposition datasets are available in supplementary information.

To further elucidate the behavior of the proposed multi-scale variational flow block during microstructure evolution prediction, we visualize the learned flow fields, masks, and routing vectors for both grain growth and spinodal decomposition in figure 2. For grain growth, figure 2(a) and 2(b) display the bidirectional flow fields $f_{t+1 \rightarrow t-1}$, and $f_{t+1 \rightarrow t}$, respectively. The flow directions and magnitudes are encoded using a standard color wheel, as shown in figure 2(c). These visualizations reveal that the network learns coherent displacement patterns aligned with the curvature-driven motion of grain boundaries. Regions with higher misorientation gradients exhibit stronger

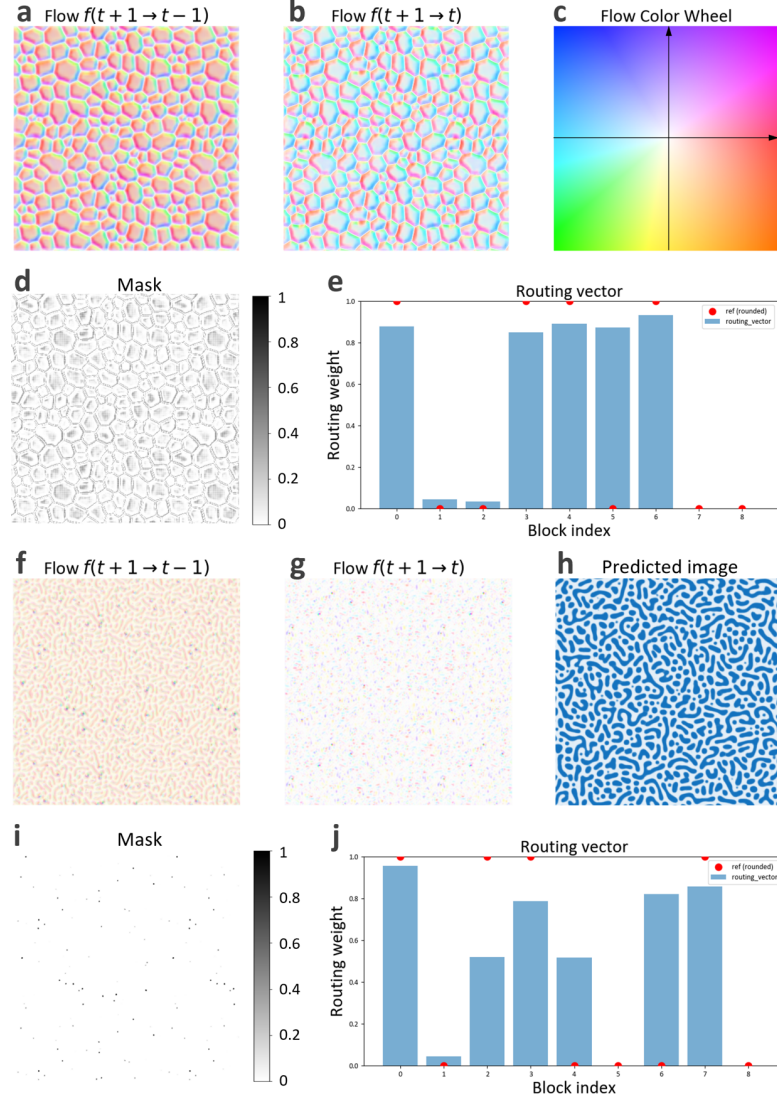


Figure 2: Visualization of intermediate voxel flow variable values. In the predicting of grain growth, pictures of visualization of flow (a) $f_{t+1 \rightarrow t-1}$, and (b) $f_{t+1 \rightarrow t}$, under (c) the color wheel, where color represents direction and magnitude of flow. (d) Mask m , (e) routing vector and rounded ref value of grain growth prediction. Also in the predicting of spinodal decomposition, pictures of flow visualization (f) $f_{t+1 \rightarrow t-1}$, and (g) $f_{t+1 \rightarrow t}$, and (h) the predicted image of the same step. (i) Mask m and (e) routing vector and rounded ref value.

flow intensities, indicating that the model internally represents the physical tendency of grains to shrink or expand.

The corresponding mask m in figure 2(d) illustrates the model’s spatial confidence in applying the flow-based warping. High-value regions correlate with active interface migration zones, whereas low-value regions suppress unreliable flow propagation, ensuring numerical stability. The routing vector and its rounded reference values in figure 2(e) further show how the model adaptively weights competing flow hypotheses. Each spatial location selects the most plausible flow direction, effectively acting as a local decision mechanism to refine the predicted microstructure.

A similar pattern is observed in the spinodal decomposition case. The predicted flow fields $f_{t+1 \rightarrow t-1}$, and $f_{t+1 \rightarrow t}$, shown in figure 2(f) and 2(g), capture the characteristic phase-separation dynamics, with flow directions pointing toward regions of compositional coarsening. The predicted microstructure at $t+1$ is shown in figure 2(h), which closely aligns with the physical evolution trend implied by the flow. The mask in figure 2(i) again selectively highlights dynamically active regions, and the corresponding routing vector 2(j) demonstrates how the model resolves ambiguity between multiple candidate flow pathways.

3. Results and Discussion

3.1. Voxel flow network prediction of phase field snapshots

We applied the VFN to predict grain growth and spinodal decomposition phase field models, with predicted results in figure 3. For both phase field models’ snapshot images, the resolution was 512×512 , and the interval between successive phase-field snapshots was 1,000 time steps. For inputs, the model was provided with two simulation images separated by 1,000 time steps. Then the network predicted 18 consecutive images, corresponding to 18,000 phase-field time steps.

3.1.1. Grain growth prediction results

For grain growth phase field model prediction, the initial configuration contained 112 grains, shown in the left rectangle in figure 3(a). After 18 predicted images, grain number decreased from 112 to 88. Three representative images of both prediction and PF simulation are shown in the right side of figure 3(a). Predicted results are displayed on the top row, aligned vertically with their corresponding ground-truth simulations on the bottom row. The

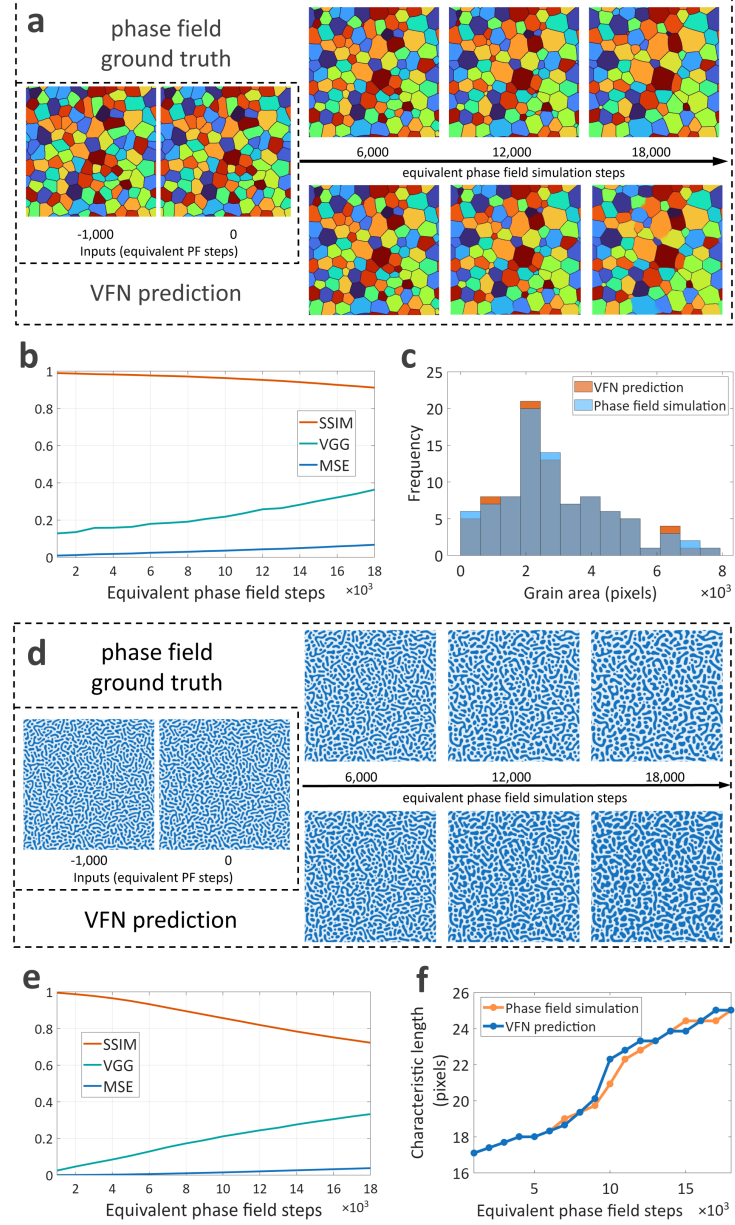


Figure 3: Voxel flow network prediction results. (a) Input images, ground truth and predicted images of grain growth evolution (full 18 frames in figure S3), their (b) SSIM, MSE and VGG loss plot, and (c) grain area distribution of final image by VFN prediction and phase field simulation. (d) Input images, ground truth and predicted images of spinodal decomposition evolution (full 18 frames in figure S4), their (e) SSIM, MSE and VGG loss plot, and (f) time evolution of characteristic length of spinodal pattern by VFN prediction and phase field simulation.

comparison demonstrates that the voxel flow network achieves high accuracy in predicting grain growth dynamics. Over this relatively long timescale, the predictions correctly captured key features such as grain disappearance and the migration of grain boundaries. Importantly, the detailed morphology of grain boundaries was well preserved after 24 grains vanished. Compared with similar efforts in previous studies, our results are more robust because grain identity is explicitly tracked and preserved through color mapping, thereby retaining the complete physical configuration of the grain system. Although minor defects were observed—for instance, distortions in grain shape after long prediction horizons and partial grain boundary smearing—the overall performance of the network is satisfactory. Moreover, although conceptually simple, the padding method effectively preserved the periodic boundary features in the input images, reflecting the effectiveness of the boundary treatment. We speculate that this improvement arises because voxel flows at boundaries are inherently more difficult to capture than those in interior regions.

To further quantify the accuracy of the network, we evaluated the predictions using three metrics: mean squared error (MSE), VGG perceptual loss [45], and structural similarity index (SSIM) [46]. The MSE was NOT computed in image RGB space, but computed in the extracted phase field configurations pointwise as follows. Since each point in the simulation domain belongs either to a grain interior or to a grain boundary, we defined the local error using a delta function and then aggregated it across the domain. This would give more physical information than using image MSE to reflect the prediction quality.

$$e(x, y) = \delta_{ij}(x, y), \quad \begin{cases} i = \text{phase index in predicted image at } (x, y), \\ j = \text{phase index in PF simulation at } (x, y), \end{cases} \quad (5)$$

$$\text{MSE} = \frac{1}{W \times H} \sum_{x=1}^W \sum_{y=1}^H e(x, y)^2 \quad (6)$$

For the perceptual loss, we employed the pretrained VGG19 network. SSIM values were computed using the scikit-image package [47]. The averaged results over 20 validation datasets are shown in figure 3(b). As expected, MSE increased approximately linearly with prediction length, while VGG loss increased and SSIM degraded more rapidly. This behavior likely reflects error accumulation in the iterative prediction scheme, where predicted frames are

repeatedly used as inputs for subsequent steps. After 18 predicted frames, the metrics still maintained 6.76% (MSE), 0.363 (VGG loss), and 0.911 (SSIM). Time to generate such predictions needs about 0.87 seconds, while phase field simulation of the same time interval needs about 1332 seconds on the same GPU, meaning our VFN achieved magnitudes faster in computational speed.

We also compared macroscopic statistics between the predicted configurations and their phase-field ground truths. Specifically, phase-field data were reconstructed from predicted images, and the grain area distribution was computed. A histogram of grain areas, shown in figure 3(c), compares the 18th predicted image with the corresponding simulation result. Among the 88 grains present, the distributions differed by only a magnitude of one at three histogram bins, while the total bin number was 13. This consistency demonstrates that the predicted images accurately reproduce the size and morphology of individual grains, further validating the network’s performance.

3.1.2. Comparison with other methods

We conducted a systematic comparison between the proposed VFN architecture and several representative spatiotemporal prediction methods, including ConvLSTM [48] and SimVP [39], to evaluate their capability for long-term microstructure evolution prediction. A primary advantage of the VFN lies in its lightweight model design. When trained on the same grain growth dataset, the competing methods exhibit significantly larger model sizes and higher memory demands than VFN, which restricts their practical applicability, particularly for large-scale simulations or resource-constrained computing environments. In contrast, the compact architecture of VFN enables efficient deployment without sacrificing prediction accuracy. A second key advantage of VFN is its computational efficiency in both training and inference. During training, the time required per epoch for VFN is substantially shorter than that of ConvLSTM and SimVP, reflecting the efficiency of its voxel-flow-based formulation. During inference, benchmark tests [49] further show that VFN achieves orders-of-magnitude higher frame rates than the other methods, while also requiring fewer floating-point operations (FLOPs). This high inference throughput is particularly important for long-horizon prediction tasks, where computational cost can otherwise become prohibitive.

To assess predictive performance, we compared the MSE, SSIM and VGG perceptual loss of grain growth predictions generated by the different models using OpenSTL [49] platform. Due to differences in the default model con-

Method	VFN	SimVP	ConvLSTM
MSE	6.3%	15.1%	57.7%
SSIM	0.92	0.89	0.81
VGG	0.31	0.40	0.94

Table 1: Comparison of error metrics on the 20th image. However, VFN was set to a harder 2-18 input-output setting, while the others were set to a 10-10 input-output setting.

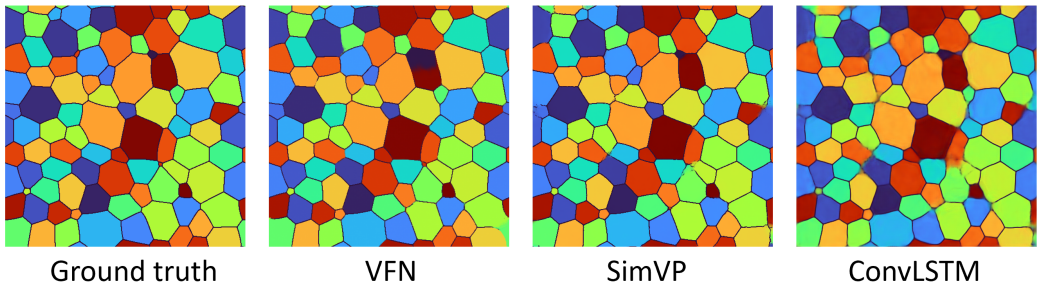


Figure 4: Comparison of the 20th snapshot between different predicting methods. VFN was set to a 2-18 input-output setting, while the others were set to a 10-10 input-output setting.

figurations, we adopted distinct input–output settings for ConvLSTM and SimVP. Specifically, these models were trained using 10 input frames to predict the subsequent 10 frames, rather than the more challenging 2-to-18 frame prediction setting used by the VFN. The predicted results, together with the corresponding ground truth, are shown in figure 4. Despite operating under a significantly more demanding prediction setting, the VFN achieves superior performance. As summarized in table 1, the VFN consistently outperforms the other models across the evaluated metrics. Although not immediately apparent in figure 4, the SimVP and ConvLSTM predictions do not consistently preserve the original grain colors, which leads to larger error metrics than might be expected.

3.1.3. Spinodal decomposition prediction results

We then extended the analysis to another phase-field model: spinodal decomposition, originally introduced by Cahn. Random initial configurations were generated, and the VFN was trained using the same procedure as for the grain growth case. The snapshot interval remained 1,000 time steps, and the image size was 512×512 . The results are shown in the same format as grain growth in figure 3(d). The VFN successfully predicted the major phase

separation process, while some detailed difference still appears compared to phase field ground truth. The coarsening of existing strips, and vanishing of small regions of phases, are captured by the model. Some topological connections between adjacent phase regions were not so accurately predicted. Then to compute quantitative metrics for error estimation, the pixel colors of predicted images were mapped to concentration values in the range (0,1) by interpolating RGB values from the colormap. The MSE was then calculated as:

$$\text{MSE} = \frac{1}{W \times H} \sum_{x=1}^W \sum_{y=1}^H (c_{\text{pred}}(x, y) - c_{\text{PF}}(x, y))^2 \quad (7)$$

VGG loss and SSIM were also computed following the same approach as for grain growth, with results shown in figure 3(e). The results at the final predicted image was 3.79% for MSE, 0.333 for VGG perceptron loss, and 0.722 for SSIM. Owing to the diffuse nature of spinodal patterns, the MSE values were lower than those for grain growth. However, SSIM scores were comparatively worse than grain growth results, reflecting the difficulty of accurately predicting fine-scale interfacial structures. In particular, the model occasionally failed to conserve the concentration ratio between the two phases, and some phase boundary shapes were not faithfully reproduced. Nevertheless, the network successfully predicted the overall long-term morphology. We then applied a 2D FFT to identify the dominant peak in the isotropic frequency domain, corresponding to the characteristic wavelength. Importantly, this key physical descriptor—the characteristic length of the spinodal pattern—was consistent between predictions and simulations, as shown in figure 3(f). Across the 18 predicted frames, the VFN reproduced the characteristic length exactly for the first six frames. The nonlinear increase observed between the 9th and 11th frames was also accurately captured, and the final predicted frame remained consistent with the ground truth.

Overall, these results confirm that the voxel flow network is capable of accurately predicting both sharp-interface and diffuse-interface microstructural evolutions across long timescales. The combination of visual agreement, quantitative metrics, and physical descriptors highlights the model’s ability to preserve key microstructural features, even under challenging conditions. At the same time, the observed deviations—particularly in long-term predictions and in concentration conservation—point to the limits of purely data-driven approaches. These findings motivate the joint strategy introduced in our methodology, where neural-network predictions are periodically corrected

with short phase-field simulations to balance efficiency and accuracy.

3.2. Joint prediction results

From the VFN prediction results, we observe that while the model achieves high accuracy for short-term evolution, errors accumulate approximately linearly with the number of predicted images. More critically, non-physical artifacts emerge, such as grain boundary dissolution at longer horizons. For example, in figure 5(a), the 38th VFN-predicted image exhibits blurred and irregular boundaries that deviate from physical expectations. To extend the predictive horizon while maintaining physical fidelity, we adopt the joint prediction scheme introduced in figure 1(b).

3.2.1. Joint prediction on 38 frames of grain growth

In this scheme, we alternate between VFN predictions and short bursts of phase field simulation, thereby stabilizing grain morphology and reducing accumulated error. Specifically, for a 38-image sequence (equivalent to 38,000 PF steps), we interleave two PF segments of 2000 steps each, producing two frames required for the next VFN input. With this setup, the prediction sequence is divided into 11 VFN - 2 PF - 11 VFN - 2 PF - 12 VFN, totaling 38 frames. Figure 5(a) compares the PF ground truth, the VFN-only prediction, and the joint prediction over the same horizon. The joint approach clearly preserves grain shape while suppressing nonphysical dissolution.

The error metrics reinforce this observation. As shown in figure 5(b), the dashed lines (VFN-only) show steady error growth, while the solid lines (joint) exhibit sharp reductions at the 12th and 25th frames, coinciding with PF insertions. Compared with VFN-only predictions, joint prediction reduces MSE from 31.89% to 9.32%, VGG loss from 0.967 to 0.409, and improves SSIM from 0.673 to 0.869. These results confirm that short PF corrections act as “error resets,” enabling stable long-term prediction without compromising efficiency.

3.2.2. Computation time cost comparison

The gain in accuracy from joint prediction naturally comes with added computational cost due to PF insertions. On an NVIDIA RTX A4000 GPU, generating one PF-equivalent frame (1000 steps) via direct PF simulation is about 100 times slower than executing one continuous VFN prediction sequence. Thus, the joint runtime depends strongly on the number of PF steps per cycle. For the 38-frame case, inserting more PF steps reduces the number

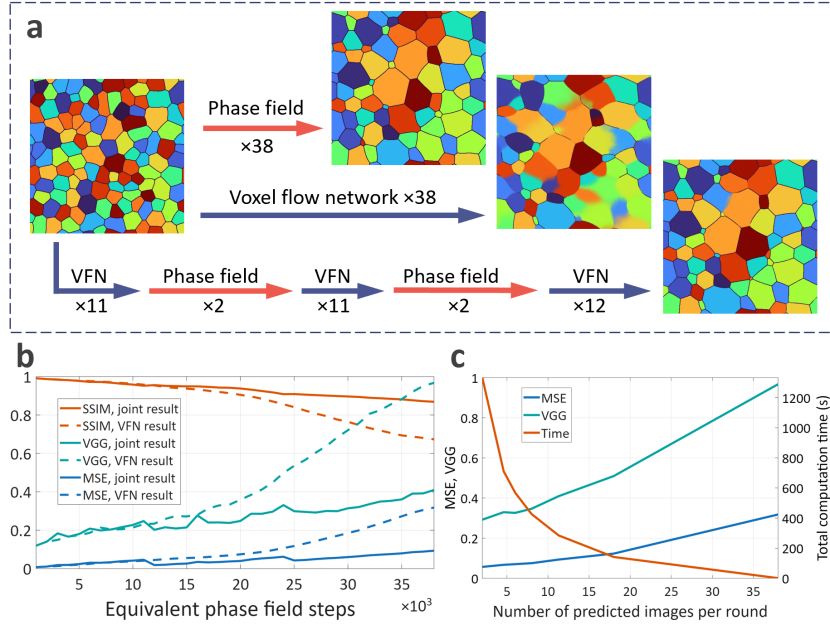


Figure 5: Joint prediction of grain growth. (a) Comparison of phase-field ground truth (red background), VFN-only prediction (blue background), and joint prediction (green background) over 38 frames. The 38th VFN-only prediction shows significant non-physical grain boundary dissolution, while the joint approach maintains grain shape and preserves physically realistic boundaries. (b) Quantitative evaluation of prediction accuracy over 38 frames using MSE, VGG perceptual loss, and SSIM. Dashed lines indicate VFN-only predictions, and solid lines indicate joint predictions. Sharp decreases in error correspond to inserted phase-field simulation segments, illustrating the corrective effect of the joint scheme. (c) Trade-off between computational cost and accuracy for varying numbers of VFN predictions per joint cycle. Increasing the number of VFN predictions per cycle reduces runtime but increases error, highlighting the balance between efficiency and precision.

of VFN frames per cycle, leading to higher costs but lower error. Additionally, because the VFN does not have the exponential effect on computation time when structure scale gets larger, the efficiency of VFN compared to phase field simulation will get even higher when simulating large domain of microstructures.

This trade-off is summarized in figure 5(c), where computation time and error metrics are plotted against the number of VFN frames per round for a constant total 38 frames. While keeping the total predicted frame equal to 38 unchanged, we change the number of frames that VFN predicts between two PF simulation segments (one PF segment always contains 2 simulated frames), which is the meaning of value on the x-axis in the figure. The more frames VFN predicts per round, the less phase field insertions will present. At $x = 38$, where no PF correction is used, computation time is minimized but error is maximized. Conversely, shorter VFN segments reduce error but increase runtime. The optimal balance occurs around 10–18 VFN steps per cycle, where accuracy is improved while maintaining substantial speedup compared with full PF simulation. Overall, the joint scheme delivers accurate, long-horizon predictions of grain growth at a fraction of the computational cost, offering a practical path for large-scale microstructure evolution modeling.

3.2.3. Joint prediction results of grain growth for ultra long time length

To further test the model’s long-horizon capability and consistency with physical evolution, we perform joint prediction for extremely long time range, with a dense initial microstructure containing 600 grains. The joint prediction model was run for 82 frames (82,000 PF steps), as total grain number decreases from 600 to 29 (which represents a huge time range), with results shown in figure 6(a). At this scale, fine-grained details differ between prediction and ground truth, but overall grain morphology and area distribution remain consistent.

Figure 6(b) shows the error metrics across the sequence. While PF insertions continue to reduce error locally, the overall growth rate of error decreases as the system coarsens. This reflects the physical fact that as grains enlarge, the evolution becomes slower and less sensitive to local fluctuations. To quantify statistical consistency, we evaluate the average grain area over time (figure 6(c)). Let y_i, \hat{y}_i be the predicted and ground truth of average grain area over time, and \bar{y} the average of \hat{y} . We calculated the NMSE of

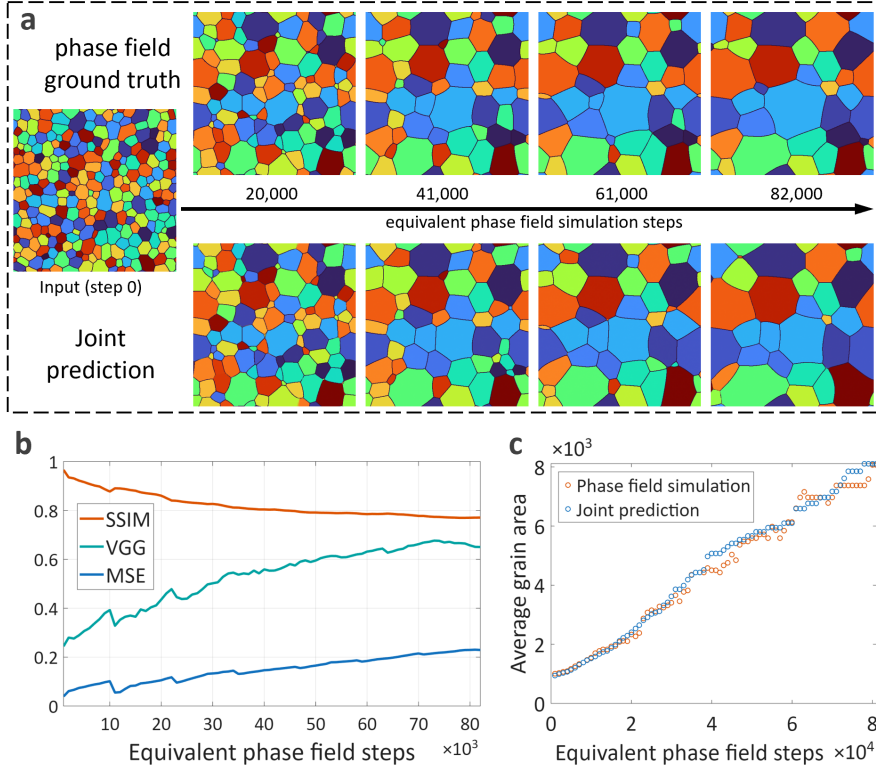


Figure 6: Long-term joint prediction for large grain microstructure. (a) Comparison of phase-field simulation (bottom) and joint-predicted (top) configurations for an initial microstructure containing 600 grains over 82 frames (full 82 frames in figure S5). Fine-grained details differ, but overall grain morphology and area distribution are well preserved. (b) Prediction error metrics (MSE, VGG loss, and SSIM) over 82 frames. Phase-field insertions reduce error locally, while the error growth rate decreases over time as grain coarsening slows the dynamics. (c) Statistical comparison of average grain area between phase-field simulation and joint prediction. Early evolution (frames 1–30) matches closely, while later evolution (frames 31–82) exhibits small oscillations due to discrete grain elimination events. Overall, the joint prediction captures the long-term trend and variability accurately.

predicted average grain area following equation (8):

$$\text{NMSE} = \frac{\sum_{i=1}^n (y_i - \hat{y}_i)^2}{\sum_{i=1}^n (y_i - \bar{y})^2} = 1.64\% \quad (8)$$

This proves that the trend of grain growth is well captured. Observing more specifically on the plot, the average grain area grows from 437 to 8687 pixels across the evolution. For the first 30 frames, joint and PF results match almost perfectly. Beyond 30 frames, the two curves oscillate but follow the same overall growth trend. The oscillations arise from discrete grain elimination events, which produce plateau-jump behavior in grain area statistics. Importantly, the joint framework captures both the trend and variability, demonstrating its robustness for long-term predictions.

4. Conclusion

In this work, we developed a joint prediction framework for phase-field microstructure evolution that combines a voxel flow network with intermittent phase-field simulations to control error accumulation and extend the prediction horizon. This joint framework operates solely on images as input, yet it is capable of recognizing and extracting the underlying physical variables of the phase field, enabling further quantitative analysis or downstream operations. Color representation of different phases achieves the full record of phase field configuration and allows joint simulation of VFN and PF method.

For direct VFN predictions, it keeps 6.76% and 3.79% MSE for grain growth and spinodal decomposition evolution after 18,000 phase field steps, while grain number decreased from 112 to 88 and spinodal pattern’s characteristic length rises from 17 to 25 pixels during this process. The VFN-based predictions achieve a substantial computational speedup, performing $10^2 \sim 10^3$ times faster than equivalent phase-field simulations on the same hardware. By carefully balancing computation time and prediction accuracy, our joint approach produces statistically reliable predictions for 82,000 phase-field time steps while requiring only 14.6% of the computational cost of a full simulation. These results demonstrate that the method can accurately capture both sharp-interface grain growth and diffuse-interface spinodal decomposition over long timescales, while preserving key physical descriptors such as grain boundary morphology, grain area distribution, and characteristic length of patterns.

This work presents an innovative, image-driven approach for microstructure prediction, significantly reducing computational time compared to traditional phase-field simulations, while maintaining physical accuracy. By incorporating phase-field corrections at regular intervals, our method effectively mitigates error accumulation over long time periods, enabling precise long-term predictions that were previously unattainable with purely machine learning-based approaches, also achieving higher generalizability than PINNs that requires pre-defined phase field models. Moreover, the image-based nature of our model offers exciting opportunities for real-time analysis of experimental microstructures, enabling direct forecasting of evolution from EBSD or SEM images with minimal pre-processing. This capability facilitates the design and optimization of materials with tailored properties based on real-world imaging data. Compared to prior studies, our joint approach considerably extends the prediction horizon while ensuring accuracy, providing a practical solution for large-scale and long-term microstructural modeling.

Looking forward, several avenues for further research are evident. First, because of the limitations of image representation of phase field data, we wish to extend the VFN’s core to a specific phase field adapted prediction module. Second, applying this joint approach to real material systems will test its robustness and utility for experimental microstructure prediction. Third, extending the methodology to more complex, multi-physics phase-field models—including systems with coupled chemical, mechanical, or thermal effects—will broaden its applicability. Finally, integrating adaptive or self-correcting strategies, such as dynamically selecting the number of VFN predictions before each phase-field insertion based on error estimates, could further improve both efficiency and accuracy. Overall, this work establishes a versatile framework that bridges data-driven prediction and physics-based simulation, opening the door to rapid, reliable, and interpretable microstructure modeling across diverse materials systems.

5. Acknowledgments

The authors would like to acknowledge the funding by the Science and Technology Commission of Shanghai Municipality (25DZ3001902, 23TS1401600). The computations in this paper were run on the Siyuan-1 and Zhiyuan-1 clusters supported by the Center for High Performance Computing at Shanghai Jiao Tong University.

References

- [1] I. Steinbach, Phase-field models in materials science, *Modelling and simulation in materials science and engineering* 17 (7) (2009) 073001.
- [2] J. Hötzer, M. Seiz, M. Kellner, W. Rheinheimer, B. Nestler, Phase-field simulation of solid state sintering, *Acta Materialia* 164 (2019) 184–195.
- [3] L.-Q. Chen, W. Yang, Computer simulation of the domain dynamics of a quenched system with a large number of nonconserved order parameters: The grain-growth kinetics, *Physical Review B* 50 (21) (1994) 15752.
- [4] L. Chen, H. W. Zhang, L. Y. Liang, Z. Liu, Y. Qi, P. Lu, J. Chen, L.-Q. Chen, Modulation of dendritic patterns during electrodeposition: A nonlinear phase-field model, *Journal of Power Sources* 300 (2015) 376–385.
- [5] Y. Shibuta, Y. Okajima, T. Suzuki, Phase-field modeling for electrodeposition process, *Science and Technology of Advanced Materials* 8 (6) (2007) 511.
- [6] J. W. Cahn, On spinodal decomposition, *Acta metallurgica* 9 (9) (1961) 795–801.
- [7] D. Tourret, H. Liu, J. LLorca, Phase-field modeling of microstructure evolution: Recent applications, perspectives and challenges, *Progress in Materials Science* 123 (2022) 100810.
- [8] Z.-H. Shen, J.-J. Wang, J.-Y. Jiang, S. X. Huang, Y.-H. Lin, C.-W. Nan, L.-Q. Chen, Y. Shen, Phase-field modeling and machine learning of electric-thermal-mechanical breakdown of polymer-based dielectrics, *Nature communications* 10 (1) (2019) 1843.
- [9] Z. Wang, W. Yang, L. Xiang, X. Wang, Y. Zhao, Y. Xiao, P. Liu, Y. Liu, M. Banu, O. Zikanov, et al., Multi-input convolutional network for ultrafast simulation of field evolvement, *Patterns* 3 (6) (2022) 100494.
- [10] M. Raissi, P. Perdikaris, G. Karniadakis, Physics-informed neural networks: A deep learning framework for solving forward and inverse problems involving nonlinear partial differential equations, *Journal of Computational Physics* 378 (2019) 686–707.

- [11] D. Lanzoni, A. Fantasia, R. Bergamaschini, O. Pierre-Louis, F. Montalenti, Extreme time extrapolation capabilities and thermodynamic consistency of physics-inspired neural networks for the 3d microstructure evolution of materials via cahn–hilliard flow, *Machine Learning: Science and Technology* 5 (4) (2024) 045017.
- [12] W. Colby L, J. Zhao, Solving allen-cahn and cahn-hilliard equations using the adaptive physics informed neural networks, *Communications in Computational Physics* 29 (2021) 930–954.
- [13] N. Haridasan, V. S. Krishnaveni, S. Sandra, M. S. Abhijith, *Physics Informed Neural Networks: Fundamentals and Application to Phase Field Models*, Springer Nature Switzerland, Cham, 2025, pp. 103–153.
- [14] P. Chen, B. Jiang, Physics-informed neural networks for learning allen-cahn equation using hard constraint representation, in: 2024 China Automation Congress (CAC), 2024, pp. 6433–6438.
- [15] N. Chen, S. Lucarini, R. Ma, A. Chen, C. Cui, Pf-pinn: Physics-informed neural networks for solving coupled allen-cahn and cahn-hilliard phase field equations, *Journal of Computational Physics* 529 (2025) 113843.
- [16] R. Qiu, R. Huang, Y. Xiao, J. Wang, Z. Zhang, J. Yue, Z. Zeng, Y. Wang, Physics-informed neural networks for phase-field method in two-phase flow, *Physics of Fluids* 34 (5) (2022) 052109.
- [17] S. Elfetni, R. D. Kamachali, Pinns-mpf: A physics-informed neural network framework for multi-phase-field simulation of interface dynamics, *Engineering Analysis with Boundary Elements* 176 (2025) 106200.
- [18] S. Elfetni, R. Darvishi Kamachali, Pinn-phase: A physics-informed neural network hybrid framework for energy-based transfer learning in diffuse interface problems, Available at SSRN: <https://ssrn.com/abstract=52070411> (2025).
- [19] W. Li, M. Z. Bazant, J. Zhu, Phase-field deeponet: Physics-informed deep operator neural network for fast simulations of pattern formation governed by gradient flows of free-energy functionals, *Computer Methods in Applied Mechanics and Engineering* 416 (2023) 116299.

- [20] G. Gangmei, S. Rana, B. Rolfe, K. Mitra, S. Bhattacharyya, Learning coupled allen-cahn and cahn-hilliard phase-field equations using physics-informed neural operator(pino) (2025). arXiv:2507.18731.
- [21] L.-C. Lin, S.-J. Chen, H.-Y. Yu, Connecting structural characteristics and material properties in phase-separating polymer solutions: Phase-field modeling and physics-informed neural networks, *Polymers* 15 (24) (2023) 4711.
- [22] A. A. K. Farizhandi, M. Mamivand, Spatiotemporal prediction of microstructure evolution with predictive recurrent neural network, *Computational Materials Science* 223 (2023) 112110.
- [23] C. Zhu, S. Liu, Z. Gao, L. Wang, J. Miao, Spatiotemporal evolution of grain microstructure: A cnn perspective, *Materials Today Communications* 40 (2024) 110005.
- [24] K. Yang, Y. Cao, Y. Zhang, S. Fan, M. Tang, D. Aberg, B. Sadigh, F. Zhou, Self-supervised learning and prediction of microstructure evolution with convolutional recurrent neural networks, *Patterns* 2 (5) (2021) 100243.
- [25] S. Fan, A. L. Hitt, M. Tang, B. Sadigh, F. Zhou, Accelerate microstructure evolution simulation using graph neural networks with adaptive spatiotemporal resolution, *Machine Learning: Science and Technology* 5 (2) (2024) 025027.
- [26] Y. Qin, S. DeWitt, B. Radhakrishnan, G. Biros, Graingnn: A dynamic graph neural network for predicting 3d grain microstructure, *Journal of Computational Physics* 510 (2024) 113061.
- [27] P. Wu, A. S. Iquebal, K. Ankit, Emulating microstructural evolution during spinodal decomposition using a tensor decomposed convolutional and recurrent neural network, *Computational Materials Science* 224 (2023) 112187.
- [28] H. Mao, C. Xie, J. Pan, Q. Cao, X. Zhang, Y. Luo, Y. Du, H. Ning, Spatiotemporal prediction of solidified dendrites based on convolutional long-short-term neural network, *Materials Today Communications* 41 (2024) 110634.

- [29] N. Wang, J. Zhou, G. Guo, Y. Zhang, W. Gao, J. Wang, L. Tang, Y. Zhang, Z. Zhang, Prediction and characterization of microstructure evolution based on deep learning method and in-situ scanning electron microscope, *Materials Characterization* 204 (2023) 113230.
- [30] D. M. d. O. Zapiain, J. A. Stewart, R. Dingreville, Accelerating phase-field-based microstructure evolution predictions via surrogate models trained by machine learning methods, *npj Computational Materials* 7 (1) (2021) 3.
- [31] C. Hu, S. Martin, R. Dingreville, Accelerating phase-field predictions via recurrent neural networks learning the microstructure evolution in latent space, *Computer Methods in Applied Mechanics and Engineering* 397 (2022) 115128.
- [32] V. Oommen, K. Shukla, S. Goswami, R. Dingreville, G. E. Karniadakis, Learning two-phase microstructure evolution using neural operators and autoencoder architectures, *npj Computational Materials* 8 (1) (2022) 190.
- [33] D. Ciesielski, Y. Li, S. Hu, E. King, J. Corbey, P. Stinis, Deep operator network surrogate for phase-field modeling of metal grain growth during solidification, *Computational Materials Science* 246 (2025) 113417.
- [34] B.-Y. Tseng, C.-W. C. Guo, Y.-C. Chien, J.-P. Wang, C.-H. Yu, Deep learning model to predict ice crystal growth, *Advanced Science* 10 (21) (2023) 2207731.
- [35] S.-J. Chen, H.-Y. Yu, L-mau: A multivariate time-series network for predicting the cahn-hilliard microstructure evolutions via low-dimensional approaches, *Computer Physics Communications* 305 (2024) 109342.
- [36] L. H. Rieger, K. Zelič, I. Mele, T. Katrašnik, A. Bhowmik, Setting the standard for machine learning in phase field prediction: a benchmark dataset and baseline metrics, *Scientific data* 11 (1) (2024) 1275.
- [37] I. Peivaste, N. H. Siboni, G. Alahyarizadeh, R. Ghaderi, B. Svendsen, D. Raabe, J. R. Mianroodi, Machine-learning-based surrogate modeling of microstructure evolution using phase-field, *Computational Materials Science* 214 (2022) 111750.

- [38] W. Yan, J. Melville, V. Yadav, K. Everett, L. Yang, M. S. Kesler, A. R. Krause, M. R. Tonks, J. B. Harley, A novel physics-regularized interpretable machine learning model for grain growth, *Materials & Design* 222 (2022) 111032.
- [39] Z. Gao, C. Tan, L. Wu, S. Z. Li, Simvp: Simpler yet better video prediction, in: *Proceedings of the IEEE/CVF conference on computer vision and pattern recognition*, 2022, p. 3170–3180.
- [40] P. Wu, H. Huang, Q. Yang, B. Qian, Y. Gao, Y. Yang, H. Zhang, Q. Zhen, Simgate: A deep learning surrogate model for predicting microstructure evolution using the phase-field method, *Computational Materials Science* 256 (2025) 113883.
- [41] X. Hu, Z. Huang, A. Huang, J. Xu, S. Zhou, A dynamic multi-scale voxel flow network for video prediction, in: *Proceedings of the IEEE/CVF Conference on Computer Vision and Pattern Recognition (CVPR)*, 2023, pp. 6121–6131.
- [42] H. X. Zhu, S. M. Thorpe, A. H. Windle, The geometrical properties of irregular two-dimensional voronoi tessellations, *Philosophical Magazine A* 81 (12) (2007) 2765–2783.
- [43] A. Paszke, S. Gross, F. Massa, A. Lerer, J. Bradbury, G. Chanan, T. Killeen, Z. Lin, N. Gimelshein, L. Antiga, A. Desmaison, A. Kopf, E. Yang, Z. DeVito, M. Raison, A. Tejani, S. Chilamkurthy, B. Steiner, L. Fang, J. Bai, S. Chintala, Pytorch: An imperative style, high-performance deep learning library, in: *Advances in Neural Information Processing Systems* 32, 2019.
- [44] C. R. Harris, K. J. Millman, S. J. van der Walt, R. Gommers, P. Virtanen, D. Cournapeau, E. Wieser, J. Taylor, S. Berg, N. J. Smith, R. Kern, M. Picus, S. Hoyer, M. H. van Kerkwijk, M. Brett, A. Haldane, J. F. del Río, M. Wiebe, P. Peterson, P. Gérard-Marchant, K. Sheppard, T. Reddy, W. Weckesser, H. Abbasi, C. Gohlke, T. E. Oliphant, Array programming with NumPy, *Nature* 585 (7825) (2020) 357–362.
- [45] J. Johnson, A. Alahi, L. Fei-Fei, Perceptual losses for real-time style transfer and super-resolution, in: B. Leibe, J. Matas, N. Sebe,

M. Welling (Eds.), Computer Vision – ECCV 2016, Springer International Publishing, Cham, 2016, pp. 694–711.

- [46] Z. Wang, A. Bovik, H. Sheikh, E. Simoncelli, Image quality assessment: from error visibility to structural similarity, *IEEE Transactions on Image Processing* 13 (4) (2004) 600–612.
- [47] S. van der Walt, J. L. Schönberger, J. Nunez-Iglesias, F. Boulogne, J. D. Warner, N. Yager, E. Gouillart, T. Yu, the scikit-image contributors, scikit-image: image processing in Python, *PeerJ* 2 (2014) e453.
- [48] X. Shi, Z. Chen, H. Wang, D.-Y. Yeung, W.-K. Wong, W.-c. Woo, Convolutional lstm network: A machine learning approach for precipitation nowcasting, *Advances in neural information processing systems* 28 (2015).
- [49] C. Tan, S. Li, Z. Gao, W. Guan, Z. Wang, Z. Liu, L. Wu, S. Z. Li, Openstl: A comprehensive benchmark of spatio-temporal predictive learning, in: Conference on Neural Information Processing Systems Datasets and Benchmarks Track, 2023.